

Tracking Large-scale Shared Bikes with Inertial Motion Learning in GNSS Blocked Environments

Feng Liu, Kejia Li, Zhiwei Yang, Chunwei Yang, Qun Li, Guobin Wu, Qiang Ni, Ruipeng Gao*

Abstract—Although Global Navigation Satellite Systems (GNSS) provide a general solution for bike tracking outdoors, there still exist complex riding environments where only inertial navigation systems work, such as urban canyons. Despite decades of research, localization using only low-cost inertial sensors still faces challenges such as cumulative drifts and poor robustness caused by filtering methods. Furthermore, sensors such as visual and LiDAR could provide reliable measurements, but they are not suitable for large-scale deployment. In this paper, we propose an inertial tracking framework that integrates bicycle mechanical constraints with a mixture-of-experts model. Specifically, we leverage multiple expert modules to capture shared representations and weight them through the gating mechanism, thus improving multi-task learning performance and enabling uncertainty-aware trajectory estimation. Furthermore, based on the mechanical transmission between the pedal and the rear wheel of a bike, we explore the intrinsic relationship between the rider’s periodic pedalling behaviors and acceleration variations, and convert such patterns into bike’s wheel speed for dynamic calibration. Experiments with real-world riding data from shared bikes of the DiDi ride-hailing platform demonstrate that our system improves the accuracy of baselines by at least 12%, with wheel speed errors below $0.5m/s$ at 95-percentile.

Index Terms—Shared bike localization, mixture-of-experts, wheel speed estimation, learning from mobile sensor data, error modelling.

I. INTRODUCTION

SHARED bikes have become a key solution to the “last mile” transportation problem in urban cities due to the flexibility, low cost, and sustainability. Thanks to the prevalence of Global Navigation Satellite Systems (GNSS) and embedded devices, we can access and track shared bikes in most urban areas. Such information is essential for bicycle location-based services, including bike retrieval, route planning, and dispatch management. However, whenever we ride through satellite blocked areas (Figure 1), such as dense building complexes, multi-level flyovers, and tree-lined roads, we lose the location awareness.

Enabling stable bike tracking in GNSS blocked environments is crucial for users to lock the device and pay the bill, as well as for ride-hailing platforms to dispatch and manage

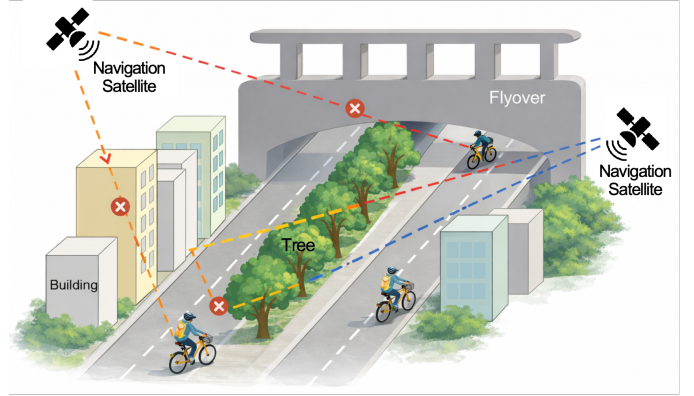


Fig. 1. Satellite signals may be blocked or even unavailable in many bike-riding environments, e.g., dense building complexes, multi-level flyovers, and tree-lined roads.

millions of shared bikes. For example, when a user returns a shared bike, the platform must determine whether it is parked in correct region. Put simply, shared bikes need to be always aware of their spatial position in the environment.

However, tracking shared bicycles in scenarios without GNSS signals is far from straightforward. Inertial Measurement Unit (IMU) provides high-frequency motion observations independent of the environment, but integration is vulnerable to severe drifts due to sensor noises, zero bias, and error accumulations. Although the Integrated Navigation System (INS) employs algorithms such as the Kalman filter [1] to fuse the absolute position from GNSS with the real-time motion from the IMU, thus suppressing inertial accumulation errors, it remains susceptible to failure in urban environments with signal blockages. Mainstream indoor localization approaches leverage Radio-Frequency signals such as Wi-Fi [2], Bluetooth [3], and Ultra-wideband [4], which are cost-expensive to deploy widely and calibrate automatically for industry. The low-cost, low-power embedded devices equipped on shared bikes constrain the types and quality of sensing modality, thus impedes the performance of real-time localization.

To address the issue of cumulative errors, some studies have proposed deep learning methods that directly regress velocity or displacement from inertial sequences, to avoid double integration, such as IONet [5], RoNIN [6], and LLIO [7]. However, these approaches typically rely on common latent features, with fixed task-specific outputs, which limits their capacity to capture unique yet correlated relationships between different tasks. In contrast, we further decompose the task, treating motion changes and their corresponding residuals and uncertainties as interrelated yet distinct tasks. Alternatively, some methods design specific error constraints

Corresponding author: Ruipeng Gao.

Feng Liu and Kejia Li are with the School of Software Engineering, Beijing Jiaotong University, Beijing 100044, China. Email: {liu.feng, kejiali}@bjtu.edu.cn.

Ruipeng Gao is with the School of Cyberspace Science and Technology, Beijing Jiaotong University, Beijing 100044, China. Email: rp-gao@bjtu.edu.cn.

Zhiwei Yang, Chunwei Yang, Qun Li and Guobin Wu are with DiDi, Beijing 100000, China. Email: {yangzhiwei, chunweiyang, liquantracy, wuguobin}@didiglobal.com.

Qiang Ni is with the School of Computing and Communications, Lancaster University, Lancaster, LA1 4WA, UK. E-mail: q.ni@lancaster.ac.uk.

based on domain-specific knowledge, using techniques such as stationary detection [8] and map matching [9] to correct errors. Nevertheless, they largely rely on specific assumptions or additional information, which are not suitable for large-scale deployment.

In order to improve the localization performance of an inertial-only dead-reckoning system, we also need to calibrate cumulative errors from long-term drifts. Such inertia-only solutions face multiple challenges in practice. First, the low-cost IMUs embedded in shared bikes are plagued by severe noises, causing unbounded positioning errors in double integrations. Second, inertial dead-reckoning inherently involves uncertainty accumulation, thus we need to calculate the uncertainty of such estimates. Finally, without GNSS signals, shared bikes lack effective measurements for calibration, thus resulting in accumulated errors during tracking.

To address such challenges, our main intuition is to discover periodic fluctuations in inertial readings during riding, which are influenced by the mechanical transmission between the bike pedal and the rear wheel, and are similar to the periodic biomechanical patterns reported in [10]. Specifically, we identify such periodic patterns in forwarding accelerations, which approximate the bicycle wheel speed. This observation enables calibration of the bike’s speed estimates in real time, thus it is referred to as “pseudo wheel speed”. In addition, we design a Mixture-of-Experts (MoE) based inertial learning model to capture potential correlations across different tasks, thus improving localization accuracy and robustness.

In sum, our contributions include:

- We propose a Multi-Task Inertial Motion Network (MTIMNet) that leverages a mixture-of-experts architecture to learn bike’s motion representations. We also estimate the prediction errors in real time to ensure interpretability for the service.
- We propose a kinematically inspired wheel speed estimation method. It detects periodic patterns in forwarding accelerations to directly derive bike’s velocity, achieving dynamic calibration without relying on additional sensors or machine learning models.
- We implement an integrated prototype and conduct extensive evaluations on real-world riding data collected by a modern ride-hailing platform. Results demonstrate that our solution outperforms baselines, achieving at least a 12% improvement in both Absolute Trajectory Error (ATE) and Absolute Yaw Error (AYE).

The rest of this paper is organized as follows. Section II reviews related work in the field of localization. Section III provides preliminary background. Section IV presents an overview of our tracking framework. Section V details the design of the Multi-Task Inertial Motion Network. Section VI analyzes the feasibility of the pseudo wheel speed estimation algorithm for shared bikes. Section VII demonstrates extensive evaluation results. Section VIII concludes the paper.

II. RELATED WORK

A. Inertial navigation methods

Classic Strapdown Inertial Navigation Systems (SINS) estimate pose by integrating IMU measurements, but accumu-

lated sensor errors cause severe drift, especially for low-cost IMUs [11]. To improve the robustness of localization, recent studies employ Deep Neural Networks (DNNs) to learn motion features and relieve errors.

On one hand, some studies leverage DNNs to calibrate inertial measurement errors. For example, [12] employed a convolutional network to denoise low-quality data using high-quality references. Calib-Net [13] utilized dilated convolutions to extract spatio-temporal features for gyroscope noise compensation. Similar works [14]–[17] show that DNNs can partially suppress inertial noise, but the performance of the models remains susceptible to variations in sensors or users.

On the other hand, many studies have established data-driven inertial motion models to mitigate the accumulation errors of SINS. Some studies focus on learning local motion variables directly from IMU sequences, such as IONet [5], RIDI [18], RoNIN [6], ConvNet [19], DeepVIP [20], and LLIO [7]. Others improve representation learning and generalization through stronger structural priors, including NILoc [21], IDOL [22], CTIN [23], EqNIO [24], and Tartan IMU [25]. Others further combine learned inertial modeling with filtering or uncertainty-aware estimation, such as TLIO [26], IMUNet [27], AirIO [28], AirIMU [17], and IMO [29]. These studies show that learning-based inertial tracking remains active in recent years, with progress in motion regression, geometric modeling, and hybrid estimation. However, they are mainly developed for pedestrians, vehicles, or aerial robots, and are not tailored to the motion characteristics and deployment constraints of shared bikes.

In addition, several studies have explored multimodal fusion, employing DNNs to map multi-sensor data to poses. [30] proposed an acoustic inertial measurement system that achieves indoor localization for drones by integrating acoustic features. [31] combined a convolutional autoencoder with a Temporal Convolutional Network (TCN) to process IMU noise and estimate latitude and longitude, which are used as observations for the KF. Similarly, methods such as [32]–[34] have demonstrated that integrating visual or LiDAR sensors can further improve localization performance, which is beyond the scope of this paper.

B. Domain-Specific Knowledge

Domain-specific knowledge in inertial navigation leverages prior information from application environments and motion patterns to enhance constraints and calibrate errors. Such approaches integrate pseudo-observations or structural constraints to improve the robustness and observability of localization in weak observation or high-noise scenarios.

Pedestrian Dead Reckoning (PDR) exploits the periodic characteristics of human gait to track pedestrian positions through step detection, heading and step length estimation, and position updates [35]. Such methods typically integrate biomechanical models with IMU signal features to extract gait parameters [36], and correct drift errors in inertial tracking with stationary phase detection (e.g., zero velocity update [8], [37]). Such methods rely on pedestrian-specific motion patterns, thus their localization accuracy depends on the quality of

feature extraction, and their application scenarios are usually limited to pedestrian localization.

In addition, methods such as map matching [9] and non-holonomic constraints [38] are usually employed within navigation frameworks to constrain errors. They are able to be regarded as reliable observations in specific scenarios. However, they typically involve additional prior information, rendering them unsuitable for all situations. In this paper, we identify a unique periodic pattern in riding scenarios and exploit this pattern as auxiliary information to improve the localization accuracy of shared bikes. To the best of our knowledge, this is the first work to discover this pattern.

III. PRELIMINARY

In GNSS blocked environments, the current platform typically employs a Strapdown Inertial Navigation System (SINS) as the odometry solution for bike tracking. Specifically, the system estimates motion variables such as orientation, velocity, and position through integration of inertial measurements from the bicycle. The IMU provides the specific force $\hat{\mathbf{a}} \in \mathbb{R}^3$ and angular rate $\hat{\boldsymbol{\omega}} \in \mathbb{R}^3$, both expressed in the body frame.

$$\begin{cases} \hat{\mathbf{a}} = \mathbf{a}_b + \mathbf{R}_{w}^b \mathbf{g}_w + \mathbf{n}_a, \\ \hat{\boldsymbol{\omega}} = \boldsymbol{\omega}_b^w + \mathbf{n}_\omega. \end{cases} \quad (1)$$

where \mathbf{g}_w denotes the gravitational acceleration in the world frame, \mathbf{R}_{w}^b denotes the rotation from the world frame to the body frame, \mathbf{a}_b is the linear acceleration in the body frame, and $\boldsymbol{\omega}_b^w$ is the angular rate of the body frame relative to the world frame, expressed in the body frame. \mathbf{n}_a and \mathbf{n}_ω represent measurement errors, which include both deterministic components (i.e., bias and scale factor errors) and random noise.

Traditional inertial navigation systems directly perform double integration of accelerations to obtain position, which results in unbounded drift due to the accumulation of measurement errors. By contrast, SINS first updates attitude with accelerations and angular rates, providing accurate orientation for velocity and position integration. The specific force measurements are transformed to the world frame and integrated once to obtain velocity, which is then further integrated to estimate position. Although there are still two integrations, the attitude update significantly decreases the risk of divergence.

Intuitively, the tracking process consists of three stages: attitude update, velocity update, and position update. Assuming ideal IMU measurements without errors as in Equations (1), we have the following:

$$\begin{cases} \mathbf{R}_b^w(t + \Delta t) = \mathbf{R}_b^w(t) \Delta \mathbf{R}_t, \\ \mathbf{v}_w(t + \Delta t) = \mathbf{v}_w(t) + \int_t^{t+\Delta t} \mathbf{a}_w(\tau) d\tau, \\ \mathbf{p}_w(t + \Delta t) = \mathbf{p}_w(t) + \int_t^{t+\Delta t} \mathbf{v}_w(\tau) d\tau, \end{cases} \quad (2)$$

where

$$\begin{cases} \mathbf{a}_w(\tau) = \mathbf{R}_b^w(\tau) \mathbf{a}_b(\tau) - \mathbf{g}_w, \\ \mathbf{v}_w(\tau) = \mathbf{v}_w(t) + \int_t^\tau \mathbf{a}_w(s) ds. \end{cases} \quad (3)$$

where $\mathbf{R}_b^w(t) \in SO(3)$ denotes the rotation from the body frame to the world frame at time t , $\Delta \mathbf{R}_t \in SO(3)$ denotes

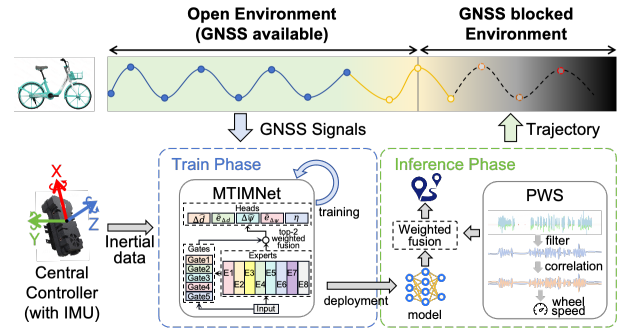


Fig. 2. Overview of the proposed inertial tracking framework for shared bikes. It consists of a Multi-Task Inertial Motion Network (MTIMNet) and a pseudo wheel speed (PWS) module. MTIMNet is trained with GNSS signals in open environments and used for GNSS-free inference, while PWS provides velocity calibration during long-term tracking.

the incremental rotation from gyroscope measurements over the interval $[t, t + \Delta t]$, and $\mathbf{g}_w \in \mathbb{R}^3$ is the gravity vector in the world frame.

Although SINS exhibits favourable interpretability, it remains dependent on the continuous propagation of attitude, velocity, and position. For generic low-cost IMUs, sensor noise, bias, scale factor errors, and mounting errors accumulate during this open-loop process, leading to rapid drift. In particular, even small attitude errors can distort gravity compensation and further amplify velocity and position errors.

To alleviate error accumulation, recent learning-based methods, such as IONet [5], RoNIN [6], and LLIO [7], reformulate inertial tracking by replacing continuous integration-based state propagation with the estimation of short-term motion updates, such as velocity, displacement, or heading increments, from fixed-window IMU sequences for incremental trajectory reconstruction. In this sense, these methods utilise learning-based alternatives to replace the integration-based motion estimation process, rather than correction modules for certain states within a conventional inertial navigation framework. Inspired by them, we regard the tracking of shared bikes in GNSS-blocked environments as a short-term inertial motion estimation task, and innovatively extract opportunistic speed observations to calibrate long-term errors.

IV. DESIGN OVERVIEW

In large-scale shared bike platforms, hardware configurations must balance manufacturing cost, maintenance efficiency, and lifecycle management. Under such constraints, shared bikes are typically equipped with a central controller integrating an IMU, a GNSS positioning module, and a mobile communications module. The communication module supports remote connectivity for data uploading and command reception. In real-world deployment, when bikes enter GNSS-blocked environments, satellite observations become unreliable, making inertial measurements the primary modality for motion estimation. However, IMU noise accumulates rapidly during integration, leading to unbounded tracking errors.

In this paper, we propose an IMU-only inertial tracking framework for shared bikes in GNSS-blocked environments. As shown in Figure 2, it consists of a multi-task inertial motion

network (MTIMNet, Section V) and a pseudo wheel speed estimation method (PWS, Section VI). The MTIMNet is trained on riding data with GNSS as ground truth in open areas, learning short-term motion variables from IMU sequences for incremental trajectory reconstruction, replacing the integration process of conventional SINS. The PWS method derives auxiliary speed observations directly from periodic pedalling patterns in accelerations without training. Thus, GNSS is used only for training supervision, whereas inference in blocked environments relies entirely on inertial measurements.

In practice, the embedded devices on shared bikes have limited computational resources and lack mature deep learning frameworks, making it difficult to execute complex models directly on the bike. Therefore, inertial readings are uploaded to remote servers at fixed intervals (e.g., every second) for model inference, while the pseudo wheel speed module runs locally on the bike. Once valid pseudo wheel speed estimates are obtained, they are fused with the output of the model using a variance-weighted method. This strategy enables effective deployment with low computational cost on the device.

V. MTIMNET DESIGN

For shared bikes, MTIMNet explores an inertial sequence learning method that leverages realtime inertial readings to infer the bike's location, with corresponding confidence assessment on such estimates.

A. Problem formulation

Based on Section III, we replace the integration-based motion estimation in conventional SINS with a learning-based estimation of short-term motion variables from IMU sequences, and progressively reconstruct the bicycle trajectory in GNSS-blocked environments. Since the task mainly involves planar motion, trajectory updates are primarily determined by displacement and heading increments, as follows:

$$\begin{cases} p_{t+\Delta t}^x = p_t^x + \Delta d_t \sin(\psi_{t+\Delta t}), \\ p_{t+\Delta t}^y = p_t^y + \Delta d_t \cos(\psi_{t+\Delta t}), \\ \psi_{t+\Delta t} = \psi_t + \Delta \psi_t. \end{cases} \quad (4)$$

where (p^x, p^y) denotes the position in the plane, Δd_t and $\Delta \psi_t$ denote the displacement and heading increment over the interval $[t, t + \Delta t]$.

In addition, IMU measurement errors are typically composed of deterministic components, including bias, scale factors, and random components such as random walk noise [11]. Existing work always approximates these errors with a Gaussian distribution. However, in practical riding scenarios, complex environments and low-cost IMUs tend to introduce additional systematic biases, such as mounting offsets or prediction bias that deviate from the Gaussian assumption. To better capture these uncertain effects, we further decompose the error sources as:

$$\varepsilon = e + \eta, \quad \eta \sim \mathcal{N}(0, \sigma^2) \quad (5)$$

where ε denotes the overall error, e represents the learnable bias, and η is an unpredictable noise term that approximately follows a Gaussian distribution. Therefore, unlike existing

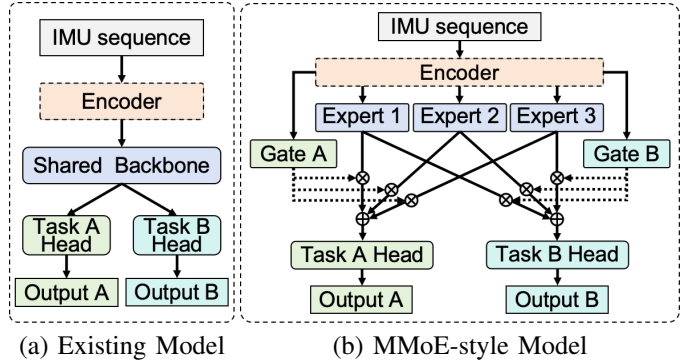


Fig. 3. Model architecture comparison between the conventional multi-head shared backbone network and the MMoE-style network.

approaches, MTIMNet leverages the residual to correct deterministic bias and captures random uncertainty by variance. The outputs for displacement and heading increments are:

$$y = \hat{y} + e + \eta \quad (6)$$

where y denotes the displacement or heading increment, \hat{y} denotes the initial estimate, e represents the residual estimate, and η denotes the uncertainty estimate. The residual term models deterministic bias, while the uncertainty term captures the remaining random error. They correspond to different error components and play different roles in the task.

B. Model structure

Existing approaches such as IONet [5], RoNIN [6], and LLIO [7] leverage DNNs to directly estimate short-term motion updates from IMU sequences, alleviating error accumulation from conventional inertial integration. However, they typically adopt a shared backbone network with similar multi-head outputs, where multiple motion-related variables are still learned from shared latent features, as shown in Figure 3(a). This coarse task decomposition may introduce interference between related tasks. Moreover, although methods such as [7], [23], [39] further estimate uncertainty together with motion updates, they do not explicitly distinguish deterministic bias from random uncertainty, which limits their ability to model the complex error characteristics of low-cost IMU data.

Recently, Multi-gate Mixture-of-Experts (MMoE) [40] has shown that different tasks in multi-task learning usually benefit from both shared features and task-specific features, rather than relying on fully shared or fully separate modeling alone. Inspired by this observation, we construct the **Multi-Task Inertial Motion Network (MTIMNet)**, which adopts the MMoE-style routing mechanism shown in Figure 3(b). Different from conventional multi-head architectures with a fixed shared backbone, MTIMNet uses shared experts to learn diverse motion features and task-specific gates to adaptively fuse them for each task, enabling more effective cross-task feature sharing while reducing interference between tasks.

The architecture of MTIMNet is illustrated in Figure 4. It consists of an inertial encoder module, multiple expert modules, multiple gating modules, and multiple task-specific heads. The encoder first maps each IMU window into latent

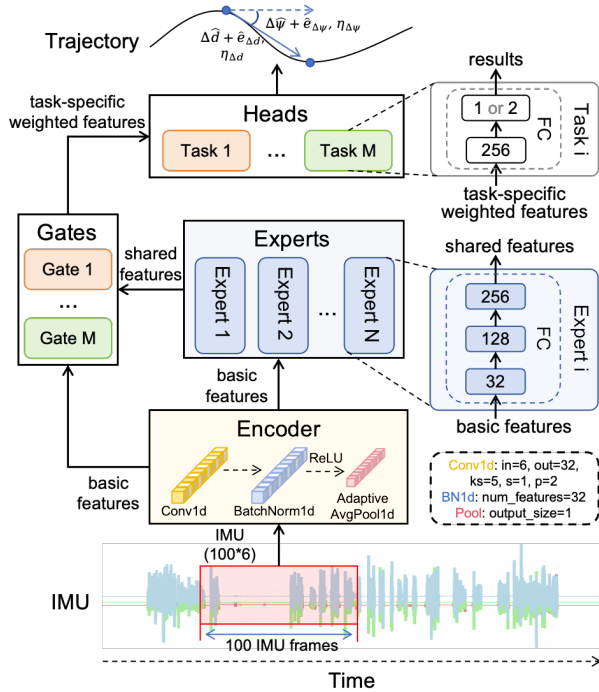


Fig. 4. Overall architecture of the MTIMNet. An encoder extracts features from IMU windows, which are processed by shared experts and task-specific gates for multi-task regression. In this paper, $M = 5$ represents five tasks, including displacement Δd and its residual $\hat{e}_{\Delta d}$, heading increment $\Delta\psi$ and its residual $\hat{e}_{\Delta\psi}$, and uncertainty η . $N = 8$ represents the number of experts.

features, which are then fed to all shared experts and task-specific gates. The experts generate candidate shared features, while the gates predict task-specific routing weights over these expert outputs. For each task, the features from the top two experts in terms of weighting will be weighted and fused, and then passed to the corresponding task head for prediction.

The **inertial encoder module** employs a stacked architecture consisting of a convolutional layer, a batch normalization layer, and an average pooling layer. The convolutional layer extracts basic local features from the inertial sequence, while the normalization and pooling layers mitigate distribution bias and reduce redundant information, respectively.

The **expert module** consists of multiple fully connected layers. We utilize eight experts to learn task-independent deep shared representations from basic features, enabling the model to capture latent patterns across different motion modes.

The **gating module** contains a fully connected layer, a softmax layer, and a dropout layer, as shown in Figure 5. It dynamically estimates the weight of each expert and obtains task-specific weighted features by fusing the features of the two experts with the highest weights. This design balances expert specialization and limited collaboration by avoiding both overly sparse single-expert routing and redundant multi-expert fusion.

The **task-specific head** exploits two fully connected layers to estimate the target from weighted features. Specifically, here are five tasks:

- Task 1: displacement Δd ,
- Task 2: heading increment $\Delta\psi$,
- Task 3: displacement residual $\hat{e}_{\Delta d}$,

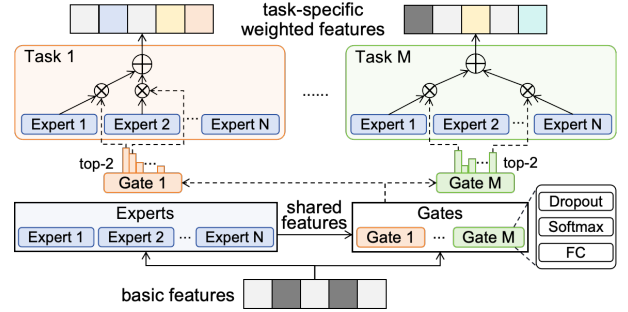


Fig. 5. Illustration of task-specific gating and top-2 expert fusion in MTIMNet. For each task, a task-specific gate predicts routing weights over all experts and fuses the outputs of top-2 experts with the highest weights.

- Task 4: heading increment residual $\hat{e}_{\Delta\psi}$,
- Task 5: uncertainty term η , consisting of $\eta_{\Delta d}$ and $\eta_{\Delta\psi}$.

Rather than deriving all task features from a single shared backbone network, MTIMNet utilises multiple experts and task-specific routing mechanisms to capture both shared and task-specific motion patterns. In practice, MTIMNet serves as a function f that maps inertial readings to motion variables within a window of Δt :

$$f(\mathbf{X}_{t-\Delta t:t}) \rightarrow (\Delta \hat{d}, \Delta \hat{\psi}, \hat{e}_{\Delta d}, \hat{e}_{\Delta\psi}, \eta_{\Delta d, \Delta\psi}) \quad (7)$$

where X denotes IMU data, and Δt represents 100 frames (1-second).

C. Loss function

We design a composite loss function to guide model training, which encourages two properties: (i) confidence-aware motion estimation, and (ii) consistency of the residual estimates. For each target $y \in \{\Delta d, \Delta\psi\}$ of a shared bike, the loss consists of two terms:

$$\mathcal{L} = \underbrace{\frac{1}{2 \exp(\eta)} \|y - \hat{y}\|^2}_{\text{Negative log-likelihood (NLL)}} + \underbrace{\frac{1}{2} \eta + L_{SmoothL1}(\hat{e}, (y - \hat{y}))}_{\text{Residual estimation loss}} \quad (8)$$

where \hat{y} and η are the mean value and log-variance of model prediction, respectively. As regressing the log-variance is more stable than directly predicting the variance [41], the first loss term adopts a negative log-likelihood formulation under the log-variance parameterization to represent model uncertainty. The second term uses Smooth L1 Loss $L_{SmoothL1}$ to minimize the difference between the predicted residual \hat{e} and its measurement $(y - \hat{y})$ for self-correction.

This formulation differs from existing multi-head regression. The residual branch models deterministic bias, while the uncertainty branch estimates the confidence of the remaining error. In this way, the MTIMNet is trained to capture deterministic and random errors separately within a unified framework. In sum, the total loss is defined as:

$$L_{total} = \sum_{y \in \{\Delta d, \Delta\psi\}} \mathcal{L}_y \quad (9)$$

To track the shard bike, we summarize the model estimate with corresponding residual to produce the final location.

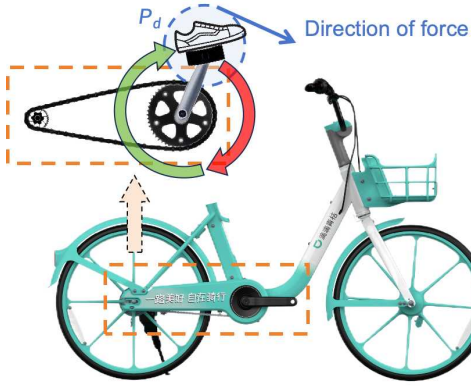


Fig. 6. Demonstration of the pedal action and one-way clutch mechanism. People exert more force in the red region than in the green region.

VI. PSEUDO WHEEL SPEED ESTIMATION

Although learning-based inertial estimation reduces the error accumulation of conventional inertial navigation, long-term inference still inevitably suffers from drift. Therefore, additional observations are needed to further constrain error growth during extended tracking, e.g., the bike velocity.

However, obtaining such observations from shared bikes always remains challenging. Sensors such as wheel odometers are difficult in large-scale deployment due to cost constraints, whereas error calibration methods (e.g., zero velocity updates [8]) exhibit dependence on specific scenarios, thus limiting their cross-scene availability. To fill this gap, we design a pseudo wheel speed estimation method that detects periodic pedalling behavior from inertial data and converts it into velocity observations for calibration, thereby constraining long-term drifts.

A. Observation: Periodic pedaling during riding

Intuitively, we observe that the force exerted during riding is not uniform, but varies systematically over the pedalling cycle, as similarly observed in [10] on muscle coordination and power output during riding. As shown in Figure 6, a rider generally exerts larger force when the pedal passes through the front region (marked as red), and less force in left region (marked as green). P_d denotes the typical position where a rider begins to exert force on the pedal.

Specifically, a one-way clutch mechanism exists between the pedal and the rear wheel of the shared bike, as indicated by the orange box in Figure 6. This means that each forward pedal rotation drives the rear wheel through a fixed number of revolutions, corresponding to an approximately constant transmission ratio K ¹, which enables wheel speed to be estimated from pedalling periodicity. In practice, mechanical resistance and bike condition may affect the conversion accuracy, but not the existence of the pedal-induced periodic pattern itself.

Thus, we calculate the rotation speed of a bike's rear wheel, i.e. the bike's velocity, from the number of pedalling cycles. Assuming that the radius of the rear wheel is r , and the time

¹In practice, the transmission ratio between pedal rotation and rear wheel rotation is generally fixed within each shared bike platform.

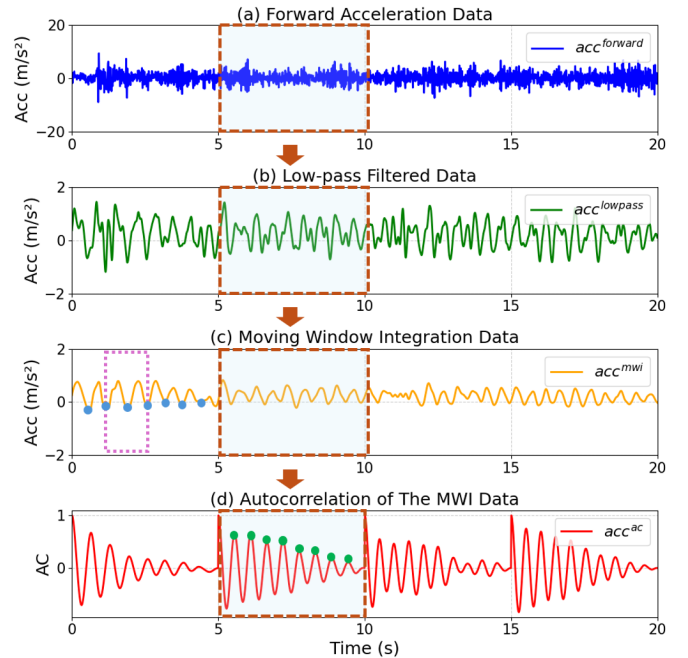


Fig. 7. Calculation process of pedalling cycles. From top to bottom: forward accelerations, low-pass filtered acceleration data, Moving Window Integration(MWI) sequence, and the autocorrelation result of the MWI sequence. We adopt a 5 seconds forward acceleration window to calculate the rider's average pedalling cycle (brown box).

for a complete pedalling cycle is T , the average speed v of the bike during this cycle is expressed as:

$$v = \frac{2\pi r K}{T} \quad (10)$$

B. Periodic detection

Calculating the pedalling cycle T is not easy, especially when tracking bikes in real time. Thus, we explore an autocorrelation-based period detection method to extract the average pedalling interval \bar{T} from forwarding accelerations.

Specifically, this period detection method mainly consists of four steps: forward acceleration calculation, low-pass filtering, moving window integration, and autocorrelation estimation, as illustrated in Figure 7.

First, we calculate the forward acceleration $acc^{forward}$ (Figure 7(a)) from the x-axis and z-axis of raw accelerations to eliminate interference from irrelevant signals, i.e.:

$$acc^{forward} = acc^z \cdot \cos \theta - acc^x \cdot \sin \theta \quad (11)$$

where θ denotes the IMU mounting angle.

Second, we denoise $acc^{forward}$ with a low-pass filter [42], yielding $acc^{lowpass}$ (Figure 7(b)).

Third, we further enhance the periodic pattern of $acc^{lowpass}$ by Moving Window Integration (MWI) [43], resulting in acc^{mwi} .

$$acc_i^{mwi} = \frac{1}{N} \sum_{j=-k}^{k-1} acc_{i+j} \quad (12)$$

where k is the half length of time window, and $N = 2k$ represents the total number of samples within this window. In our implementation, we adopt $k = 15$.

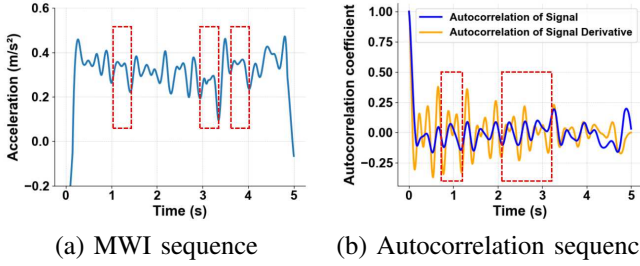


Fig. 8. The MWI and autocorrelation sequences of forward accelerations in the fast riding scenario.

Figure 7(c) briefly demonstrates the pedalling behavior of acc^{mwi} , where the purple box denotes a complete pedalling cycle. Each acceleration valley corresponds to the moment when a rider begins exerting force on the pedal, and the intervals between two acceleration valleys approximately indicate a half cycle of pedal rotation.

Finally, we compute the autocorrelation [44] of acc^{mwi} to determine its periodicity, yielding the sequence acc^{ac} (Figure 7(d)).

The interval between peaks in acc^{ac} corresponds to the period of acc^{mwi} . We calculate the time difference between adjacent peak moments to construct t_{diff} . If $\frac{\max(t_{diff})}{\min(t_{diff})} < 1.4$, the current data is considered to exhibit periodicity. Specifically, we compute the average pedalling cycle time as $\bar{T}_{acc^{mwi}} = \text{mean}(t_{diff})$, thus leading to $\bar{T} = 2 \cdot \bar{T}_{acc^{mwi}}$.

C. Anomaly detection

In practice, we observe that when a rider pedals continuously at high speeds (e.g., exceeding 4.5 m/s), the pedals may fail to simultaneously rotate with the rear wheel.

Normally, the data marked by the red box in Figure 8(a) should contain only one peak. However, the above anomaly leads to multiple peaks here. To filter such anomalies, we first calculate the derivative of acc^{mwi} , denoted as \dot{acc}^{mwi} , and then further compute autocorrelation values of \dot{acc}^{mwi} , denoted as \dot{acc}^{ac} . In abnormal scenarios, acc^{ac} and \dot{acc}^{ac} exhibit significant deviations, as illustrated in Figure 8(b). We identify these deviations with the following two methods.

- Pearson Correlation Coefficient (PCC): We exploit the Pearson correlation coefficient ρ to measure the similarity between the two autocorrelation sequences. The two signals are considered different if $\rho < 0.6$.
- Comparison of Peak Counts (CPC): We denote the number of peaks within a data window by $peaks(\cdot)$. The two signals are considered different if $\frac{peaks(\dot{acc}^{ac})}{peaks(acc^{ac})} > 1.2$.

Once a valid average pedalling period $T = \bar{T}$ is extracted from anomaly-free data, the current wheel speed can be calculated with Equation 10.

D. Fusion with MTIMNet estimation

In practice, several riding conditions may violate the steady-pedalling assumption, including reverse pedalling, coasting, downhill motion without pedalling, and other sections where

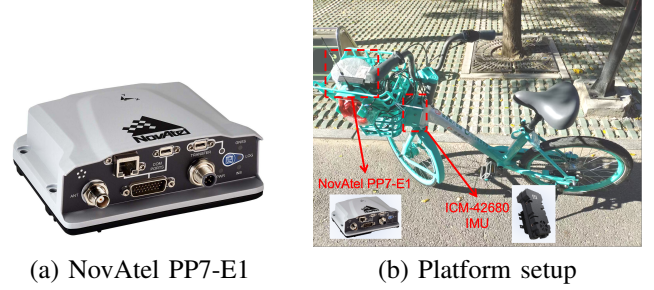


Fig. 9. NovAtel PP7-E1 device and its configuration on a bike platform for ground truth collection.

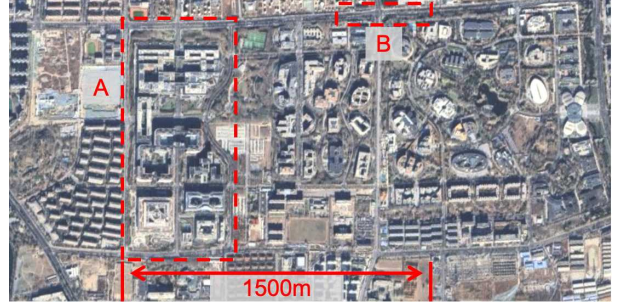


Fig. 10. Top view of the Customized Dataset collection area.

speed varies. Therefore, pseudo wheel speed is estimated only when valid periodic pedalling patterns are detected.

Once a valid pseudo wheel speed is detected², it is converted into a displacement observation over the corresponding interval and fused with the MTIMNet displacement estimate. Let \hat{d}_m and σ_m^2 be the displacement and variance predicted by MTIMNet, and let \hat{d}_p and σ_p^2 be those derived from pseudo wheel speed, where σ_p^2 is derived from the standard deviation of the speed error for different riding speed levels (i.e. slow, moderate and fast) as detailed in Section VII-F. The fused displacement is given by:

$$\hat{d}_f = \frac{\hat{d}_m/\sigma_m^2 + \hat{d}_p/\sigma_p^2}{1/\sigma_m^2 + 1/\sigma_p^2}. \quad (13)$$

This inverse-variance weighted fusion assigns a larger weight to the more reliable estimate and helps reduce long-term drift.

VII. EVALUATION

In this section, we describe detailed experiment settings and conduct evaluations based on real-world riding data collected by the DiDi ride-hailing platform.

A. Implementation & Dataset

Existing open-source inertial data sets provide insufficient coverage for bicycle motions. To validate the proposed solution, we construct multiple riding data sets covering different cities, users, and bicycles. The detailed dataset include:

²Since the proposed pseudo wheel speed is available only when effective periodic pedalling is detected, it is regarded as an auxiliary observation rather than a continuously available speed measurement.

TABLE I

INFORMATION STATISTICS FOR VOLUNTEERS OF THE PERIODIC DATASET.

Feature	Male (n=18)	Female (n=12)	Total (n=30)
Age	29.89±14.49	36.83±13.70	32.67±13.21
Height	174.06±7.07	163.42±4.48	169.80±8.06
Weight	71.42±8.81	58.33±5.51	66.18±9.98
BMI	23.63±3.13	21.88±2.30	22.93±2.91

1) **Customized Dataset:** We construct a customized bicycle platform and collect a Customized Dataset with high-precision ground truth in Beijing. The platform integrates a TDK-InvenSense ICM-42680 IMU³ and a NovAtel PP7-E1 device⁴, as shown in Figure 9. The IMU records 3-axis acceleration and angular rate, while the NovAtel device provides high-precision ground truth enhanced by differential positioning services. The platform achieves centimetre-level horizontal localization accuracy and about 0.5 degrees orientation accuracy, making it a reliable ground truth reference. To ensure consistent motion measurements, the NovAtel device is rigidly mounted in the bike basket within 20 *cm* of the IMU.

Figure 10 marks the data collection areas, covering different trajectories, environments, and times. Specifically, we collect the training, validation, and test-seen sets in Area A, and build the test-seen and test-unseen sets in Area B. The bike moved at varying speeds during data collection, with up to about 5 *m/s*. This dataset contains about 400 trajectories, each lasting 2 to 3 minutes, with a maximum distance of up to about 550 metres and a total distance of about 102 *km*. We divided the whole data into training, validation, test-seen and test-unseen sets with a ratio of 9:2:2:2.

2) **Crowdsourced Dataset:** Besides the customized platform, we further collect crowdsourced riding data in Hangzhou and Beijing by the DiDi ride-hailing platform for about two weeks, to evaluate the robustness and generalization of the solution in real-world riding environments. Specifically, we have collected inertial measurements and GNSS signals during riding on six bikes. The dataset includes trajectories from about 100 different users, with a total duration and distance of about 30 hours and 210 *km*, respectively. We divided the dataset according to the ratio of 39:8:13:11, and the rest of the data processes are similar to the Customized Dataset.

3) **Periodic Dataset:** To systematically evaluate the generalization and robustness of the pseudo wheel speed estimation module, we invite 30 volunteers to collect the Periodic Dataset. Table I presents their age, height, weight, and Body Mass Index (BMI) as mean ± standard deviation. Data are collected on a university campus across diverse riding scenarios, including multiple speed levels, free riding, riding with coasting, riding with intermittent stops, and riding with resistance under light braking. In addition to DiDi shared bikes, we also collect free riding data from other two ride-hailing platforms, i.e., Meituan Bike and Hello Bike, to evaluate the cross-platform reliability of the proposed PWS estimation method. The detailed distribution is given in Table II.

TABLE II

DATA DISTRIBUTION STATISTICS FOR THE PERIODIC DATASET

Platform	Scenarios	Mean ± Std (m/s)	Total duration (min)	Total distance (km)
DiDi	Slow	2.282 ± 0.552	54.63	7.27
	Moderate	3.062 ± 0.654	42.50	6.99
	Fast	4.149 ± 1.183	18.33	4.29
	Free	3.357 ± 0.946	94.27	19.31
	w/ Coasting w/ Stopping w/ Resistance	2.824 ± 0.649 1.869 ± 1.120 3.104 ± 0.392	10.63 14.85 20.62	1.75 1.71 3.64
Meituan	Free	3.299 ± 0.349	79.93	14.95
Hello	Free	3.451 ± 0.633	84.00	15.46
Total			419.09	75.37

B. Baselines

For the MTIMNet model, we compare it with one classical inertial dead reckoning baseline and several representative learning-based inertial localization methods, including IONet [5], RoNIN [6], LLIO [7], UniTS [45], Liu *et al.* [46], IMUNet [27], EqNIO [24], and AirIO [28]. These baselines cover recurrent, residual, temporal-convolutional, time-frequency, and recent geometry-aware or motion-adaptive architectures for inertial motion estimation. For fair comparison, all learning-based baselines are trained and evaluated under the same data split and setting.

For pseudo wheel speed (PWS) estimation, we compare it with two representative time-domain and frequency-domain periodic detection baselines respectively. The first is Peak Detection (PD), which estimates the pedalling period from the average interval between local peaks detected on the moving-window integration (MWI) signal. The second is Fast Fourier Transform (FFT)-based estimation, which transforms the MWI signal into the frequency domain and uses the dominant spectral component to infer the pedalling period.

C. Evaluation Metrics

We evaluate both localization accuracy and pseudo wheel speed estimation quality respectively. For localization, we adopt four standard metrics: Absolute Trajectory Error (ATE) [47], Relative Trajectory Error (RTE) [47], Position Drift Error (PDE) [23], and Absolute Yaw Error (AYE) [7], which measure global trajectory accuracy, local trajectory consistency, drift level, and heading accuracy, respectively. For PWS estimation, we use Circular Error Probable (CEP) to measure the deviation between the estimated wheel speed and the high-precision speed provided by the NovAtel device.

D. Performance Comparison

Evaluation on the Customized Dataset: Table III reports the quantitative comparison of all models on the Customized Dataset. MTIMNet achieves the best performance on both the test-seen and test-unseen sets. Compared with the best baseline, it improves ATE and RTE by over 13% and 14%, respectively. Furthermore, a PDE of 0.07 on the test-seen set means an average error of about 7 *cm* per meter traveled. In addition, the MTIMNet improves heading estimation accuracy

³<https://invensense.tdk.com/products/motion-tracking/6-axis/>

⁴<https://novatel.com/products/gnss-inertial-navigation-systems/combined-systems/pwrpak7-e1>

TABLE III

PERFORMANCE COMPARISON OF DIFFERENT MODELS ON THE CUSTOMIZED DATASET. RED MARKERS DENOTE THE BEST PERFORMANCE AMONG ALL METHODS, BLUE MARKERS DENOTE THE BEST PERFORMANCE AMONG ALL BASELINES, AND "IMPROVEMENT" INDICATES THE ENHANCEMENT OF RED MARKERS OVER BLUE MARKERS.

Dataset	Test subjects	Metric	DR	IONet	RoNIN	LLIO	UniTS	Liu <i>et al.</i>	IMUNet	EqNIO	AirIO	MTIMNet	Improvement
Customized Dataset	Seen	ATE	72.16	20.01	18.18	17.56	17.83	38.31	19.79	17.36	17.20	14.91	13.31% ↑
		RTE	83.73	20.42	20.03	19.02	17.89	44.28	19.53	17.93	17.94	14.23	20.46% ↑
		PDE	0.41	0.10	0.09	0.08	0.08	0.20	0.10	0.08	0.08	0.07	12.50% ↑
		AYE	11.52	4.84	3.75	3.04	3.43	11.57	3.44	3.02	3.41	2.03	32.78% ↑
	Unseen	ATE	63.02	18.45	17.18	15.85	13.82	39.54	16.15	13.43	13.26	11.46	13.57% ↑
		RTE	64.63	21.33	20.85	17.96	14.28	44.33	18.18	14.76	15.16	12.27	14.08% ↑
		PDE	0.28	0.10	0.08	0.07	0.06	0.19	0.07	0.06	0.06	0.05	16.67% ↑
		AYE	11.23	5.90	5.30	3.43	2.41	11.28	3.14	2.32	3.34	1.78	23.28% ↑

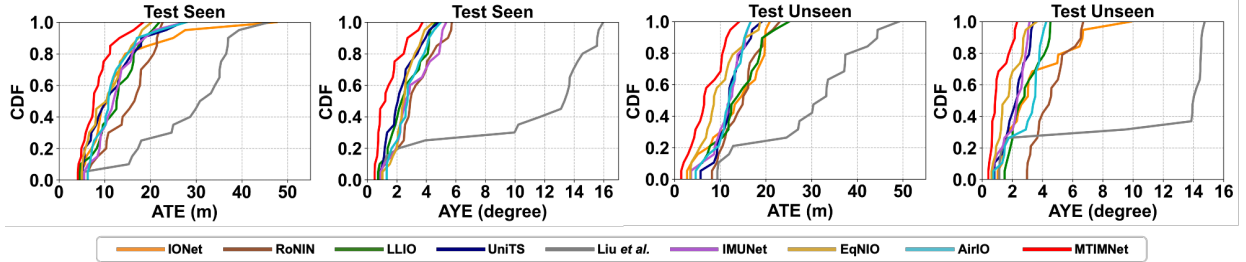


Fig. 11. ATE and AYE for different methods on the Customized Dataset. The MTIMNet model outperforms baselines on both test-seen and test-unseen sets.

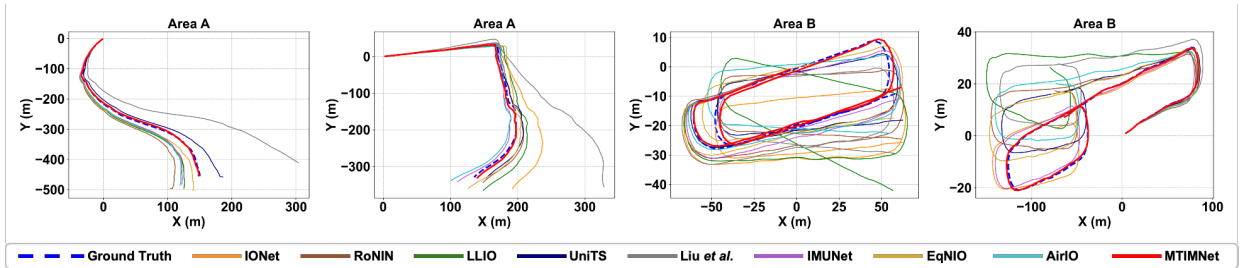


Fig. 12. Example trajectories produced by different models. Results from the MTIMNet model are closer to the ground truth.

TABLE IV

QUANTITATIVE COMPARISON OF DIFFERENT MODELS ON THE CROWDSOURCED DATASET. RED VALUES DENOTE THE BEST PERFORMANCE AMONG ALL METHODS, WHILE BLUE VALUES DENOTE THE BEST PERFORMANCE AMONG ALL BASELINES.

Dataset	Test subjects	Metric	DR	IONet	RoNIN	LLIO	UniTS	Liu <i>et al.</i>	IMUNet	EqNIO	AirIO	MTIMNet	Improvement
Crowdsourced Dataset	Seen	ATE	50.60	24.72	21.75	23.66	21.77	29.01	21.83	19.21	19.76	16.83	12.39% ↑
		RTE	59.34	27.72	24.04	26.89	25.07	31.20	24.23	21.74	22.66	18.57	14.58% ↑
		PDE	0.61	0.22	0.19	0.25	0.16	0.38	0.24	0.21	0.34	0.14	12.50% ↑
		AYE	17.74	12.35	9.12	14.30	10.77	17.81	9.38	11.29	9.45	7.75	15.02% ↑
	Unseen	ATE	44.91	22.95	21.58	26.82	19.74	27.72	21.42	20.22	19.78	16.26	17.63% ↑
		RTE	51.60	25.39	23.81	29.19	22.71	30.17	23.40	22.08	21.13	18.13	14.20% ↑
		PDE	0.51	0.26	0.21	0.28	0.19	0.38	0.29	0.23	0.35	0.15	21.05% ↑
		AYE	27.97	13.74	12.33	21.41	11.70	28.09	11.10	11.15	11.74	9.54	14.05% ↑

through adaptive expert fusion and multi-task supervision, achieving at least a 23% improvement in AYE.

Figure 11 illustrates the Cumulative Distribution Function (CDF) of ATE and AYE for different models. We observe that the MTIMNet model outperforms baseline methods on both the test-seen and test-unseen sets, thus demonstrating its robustness and accuracy. Figure 12 shows visualisations of several estimated trajectories derived from real-world riding data. The results show that the trajectories estimated by MTIMNet are closer to the ground truth, whereas baseline methods generally fail to maintain a good balance between trajectory and heading accuracy.

Evaluation on the Crowdsourced Dataset: To validate

robustness in more general scenarios, we further compare MTIMNet with the baselines on the Crowdsourced Dataset, as shown in Table IV. Although the baselines achieve acceptable accuracy, MTIMNet outperforms them on all metrics, with improvements of at least 12% in ATE and 14% in AYE. Moreover, while baseline errors increase on the more complex crowdsourced data, the MTIMNet maintains stable performance, demonstrating stronger robustness and generalization.

E. Model Performance Study

1) *Task Study:* To evaluate MTIMNet on different tasks, we compare its displacement and heading estimates with those of the best baseline, UniTS, against the ground truth. Figure 13(a)

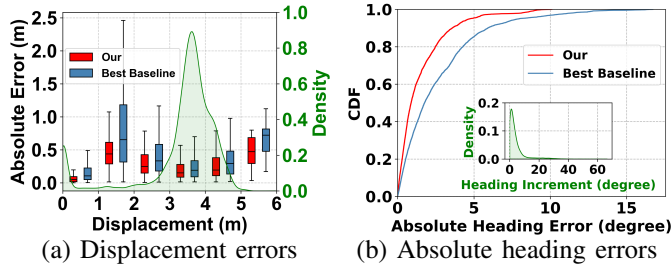


Fig. 13. Comparison of MTIMNet with the best baseline in terms of displacement and heading. The green curves show the distribution of ground truth for displacement and heading increments, respectively.

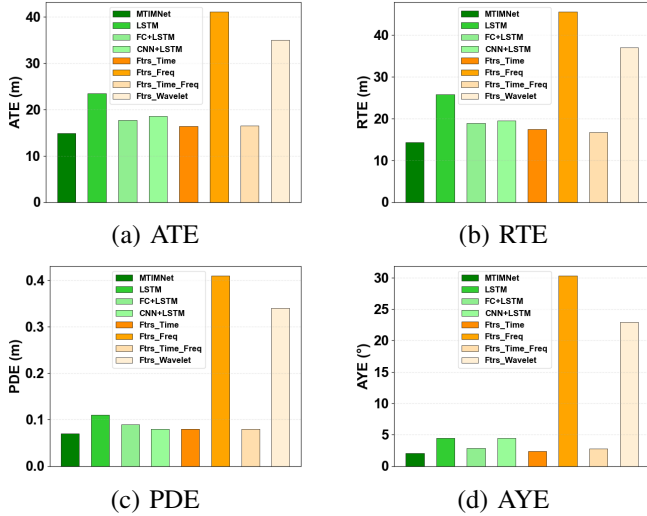


Fig. 14. Performance comparison of MTIMNet with different model structures or input features. Green bars: different network architectures. Orange bars: different input features, which are used to replace the encoder module.

shows the ground truth displacement distribution, where samples are divided into 1 metre intervals to compare displacement errors. MTIMNet yields lower displacement errors across all intervals, remaining almost always below 1 metre even when the riding speed exceeds 5 m/s.

Figure 13(b) shows the CDF of absolute heading errors for MTIMNet and the best baseline, while the inset gives the distribution of ground truth for heading increments. MTIMNet achieves higher heading accuracy while maintaining strong displacement performance, indicating that its shared experts and task-specific gating effectively balance different tasks.

2) *Model Structure Study*: In MTIMNet, the encoder extracts basic features from raw IMU sequences for the experts and gating modules. To evaluate different architectures, we compare encoders built with fully connected layers (FC), convolutional neural networks (CNN), and long short-term memory networks (LSTM), and also test a scheme that directly uses handcrafted time- and frequency-domain features from IMU readings without an encoder.

Figure 14 compares these methods on different metrics. Here, “LSTM” uses an LSTM encoder, while “FC+LSTM” and “CNN+LSTM” use FC and CNN encoders with LSTM task heads. “Ftrs_” denotes handcrafted time-, frequency-, and

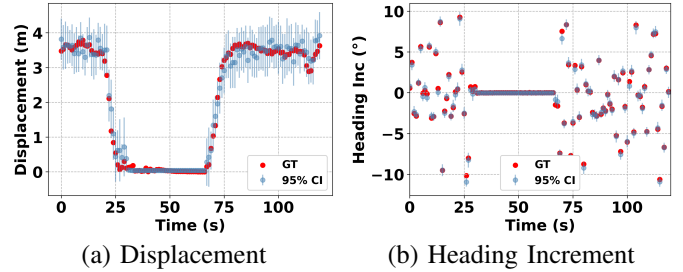


Fig. 15. Uncertainty estimation effects for different tasks. Red dots refer to ground truth, blue dots refer to model estimates, and blue lines indicate uncertainty bounds. The ground truth is almost entirely covered.

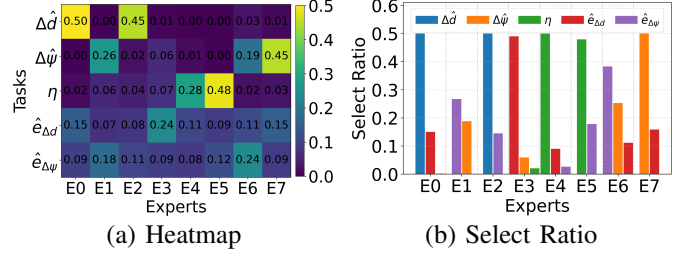


Fig. 16. Task-expert analysis of the proposed MTIMNet. (a) Average gating weights assigned to each expert for different tasks. (b) Expert selection ratios under sparse top-2 routing for different tasks.

wavelet-domain features from 6-axis IMU data.⁵ The results show that the CNN-based encoder performs best, while time-domain features are the most effective among the handcrafted alternatives.

3) *Uncertainty Study*: To validate the accuracy of the uncertainty estimates, we quantitatively evaluate the coverage of the ground truth within the estimated confidence intervals. For displacement Δd and heading increment $\Delta\psi$, we construct the 95% Confidence Interval (CI) as $CI = [\hat{y}_t - z \cdot \sigma_t, \hat{y}_t + z \cdot \sigma_t]$. \hat{y}_t denotes the estimated value of Δd and $\Delta\psi$ at moment t , σ_t is the uncertainty estimation (standard deviation), and $z=1.96$ is the standard normal quantile at the 95% confidence level. Figure 15 demonstrates the accuracy of the estimates, where the ground truth (red dots) are almost entirely contained within the uncertainty bounds from the model (blue lines). The MTIMNet model achieves uncertainty estimation coverage rates of 94.7% for Δd and 95.2% for $\Delta\psi$, which are close to the ideal 95% confidence level.

4) *MoE behavior interpretability*: To further analyze the MoE behavior, Figure 16 visualizes the expert selection patterns of different tasks. The heatmap shows the average gating weights, and the bar chart shows the frequency of each expert being selected in the top-2 routing results. Different tasks exhibit distinct expert preferences, rather than uniformly relying on the same shared representation. This indicates that the proposed model performs task-specific routing and captures partially shared yet task-dependent motion representations.

5) *Experts and Top-k Study*: To justify the expert-routing design, we compare different numbers of experts and top-

⁵“Time” includes maximum, minimum, mean, standard deviation, and integration. “Freq” includes dominant frequency, spectral entropy, energy, spectral centroid, and PSD peaks from FFT. “Wavelet” includes sub-band energy ratios extracted using the “db3” basis with three-level decomposition.

TABLE V

PERFORMANCE COMPARISON UNDER DIFFERENT NUMBERS OF EXPERTS AND TOP-K ROUTING STRATEGIES. FOR EACH SETTING, THE FIRST ROW IN EACH CELL DENOTES ATE, WHILE THE SECOND ROW DENOTES AYE.

Experts	Top-k				
	top-1	top-2	top-4	top-5	All
5	16.56	15.44	16.01	17.09	
	2.59	2.34	2.43	3.05	
8	15.31	14.91	17.61	18.55	19.03
	2.57	2.03	3.01	3.86	3.55
10	15.76	15.13	15.97	16.89	17.28
	2.44	2.32	2.52	2.70	3.30

TABLE VI

COMPARISON OF DIFFERENT PERIODIC DETECTION ALGORITHMS. THE TCR DENOTES THE RATIO OF THE TIME WHEN PSEUDO WHEEL SPEED IS DETECTED TO THE TOTAL TIME ACROSS ALL DATA.

Method	CEP68 (m/s)	CEP80 (m/s)	CEP95 (m/s)	Max (m/s)	TCR \uparrow
Ours	0.18	0.24	0.42	1.28	50.0%
PD	0.81	1.09	1.89	5.36	98.0%
FFT	0.24	0.34	1.57	3.41	54.0%

k routing strategies, as summarized in Table V. The best performance is achieved with 8 experts and top-2 routing. Fewer experts limit representation ability, whereas more experts provide no further gain. Compared with top-2, both top-1 and denser fusion perform worse, suggesting that sparse task-specific routing is more effective than dense shared fusion.

F. Pseudo Wheel Speed Estimation Performance Study

Evaluation on the Periodic Dataset: To demonstrate the effectiveness of the autocorrelation-based periodic detection method, we compared it with two baselines: the PD method and the FFT-based method, on the Periodic Dataset. Specifically, all methods run on the MWI sequences from forward acceleration data, using a 5 seconds sliding window with a 1-second step.

Table VI quantifies the overall performance of different periodic detection methods, where the Time Coverage Ratio (TCR) denotes the ratio of the time when pseudo wheel speed is detected to the total time. Our method achieves the best balance between estimation accuracy and valid detection coverage, showing that the periodic detection and anomaly filtering strategy is effective for extracting reliable pedal-induced speed observations.

Comparison in different scenarios and bike platforms:

Figure 17 summarizes the pseudo wheel speed estimation performance under different riding scenarios and across different shared bike platforms. The method maintains low speed error under stable pedalling, while the TCR decreases in fast, coasting, and stopping cases where pedalling periodicity is weak or absent, indicating that pseudo wheel speed is activated only under valid pedalling conditions. The results on riding with resistance and on Meituan Bike and Hello Bike further suggest that variations in bike condition and mechanical configuration mainly affect the estimation bias and valid detection ratio, but do not invalidate the proposed periodic detection framework.

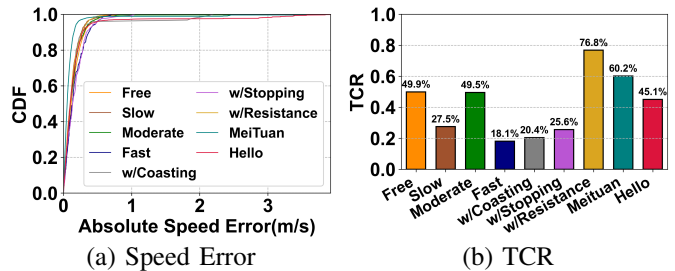


Fig. 17. Performance of pseudo wheel speed estimation under different riding scenarios and bike platforms.

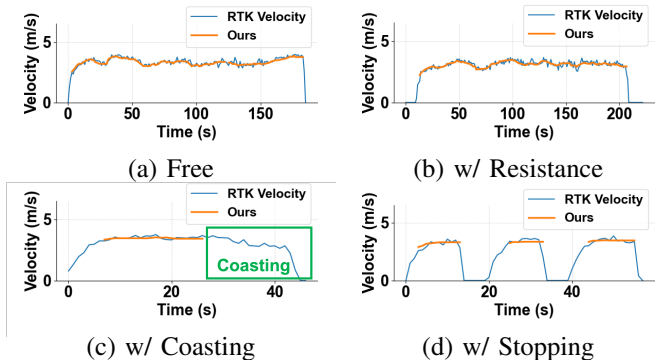


Fig. 18. Comparison of pseudo wheel speed estimation with RTK velocity in four representative riding scenarios.

Figure 18 presents the speed estimation results for four representative scenarios, including free riding, riding with resistance, riding with coasting, and riding with intermittent stops. The estimated pseudo wheel speed closely follows the RTK velocity during valid pedalling intervals, while naturally suppressing outputs during coasting or non-pedalling segments. These examples demonstrate that the pseudo wheel speed can provide sufficiently reliable auxiliary observations under periodic riding patterns.

G. Ablation Study

MTIMNet: We evaluate the effectiveness of different components in MTIMNet from four aspects, including the model structure, residual estimation, uncertainty estimation, and multi-task loss. Table VII presents the complete comparison.

1) *Model Structure:* We replace the experts and gating modules with multilayer perceptron (MLP)-, LSTM-, and TCN-based backbones, similar to IONet [5], RoNIN [6] and LLIO [7]. The performance drop across all metrics, especially in trajectory and heading errors, shows that fixed shared features are insufficient, while the proposed expert-routing design provides more suitable task-specific motion representations.

2) *Residual Estimation:* To validate the residual branch, we remove the residual estimation task and its loss term, while keeping the other components unchanged. Table VII shows consistent degradation across all metrics, with ATE increasing from 14.91 to 16.75 and AYE from 2.03 to 2.64, confirming that the residual branch helps correct prediction bias and improve accuracy.

3) *Uncertainty estimation:* To evaluate the effect of uncertainty modeling, we remove the uncertainty branch and its

TABLE VII

ABLATION STUDY OF MTIMNET ON THE CUSTOMIZED DATASET. LOWER IS BETTER FOR ALL METRICS. THE CHECKMARKS INDICATES ACTIVATED.

Variant	Modules			Error			
	Experts +Gates	Residual	Multi-task Loss	ATE (m)	RTE (m)	PDE (m)	AYE (degree)
MTIMNet (Ours)	✓	✓	✓	14.91	14.23	0.07	2.03
MLP-based		✓	✓	17.26	17.28	0.09	3.22
LSTM-based		✓	✓	16.71	17.58	0.08	4.27
TCN-based		✓	✓	18.88	19.14	0.09	4.50
w/o Residual	✓			16.75	16.23	0.08	2.64
w/o Uncertainty	✓	✓		15.47	15.42	0.07	2.14
w/o Multi-task Loss	✓	✓		16.25	16.00	0.07	2.82
w/o All				19.85	20.17	0.11	4.30

TABLE VIII

ABLATION STUDY ON PSEUDO WHEEL SPEED ESTIMATION.

Method	CEP68	CEP80	CEP95	Max	TCR ↑
w/ All	0.207	0.274	0.480	0.723	18.1%
w/o PCC	0.229	0.312	0.656	2.010	19.9%
w/o CPC	0.294	0.532	2.578	3.766	34.1%
w/o PCC & CPC	0.331	0.796	2.540	3.766	37.4%

loss term, while preserving the residual branch and the expert-routing structure. Almost all metrics exhibited degradation, suggesting that uncertainty estimation is not redundant but rather provides useful, confidence-aware guidance.

4) *Multi-task loss function*: To demonstrate the effectiveness of the loss function, we remove the residual estimation loss. Specifically, instead of learning residuals through independent tasks, we implicitly estimate the residuals in the model and compensate them to the corresponding tasks. As shown in the figure, the learning residuals implicitly result in an increase of 8% for ATE and 28% for AYE, respectively.

Pseudo Wheel Speed Estimation: To evaluate the effectiveness of the anomaly detection module, we conducted ablation experiments in the fast-riding scenario by selectively removing the two components: Pearson Correlation Coefficient (PCC) and Comparison of Peak Counts (CPC). Table VIII presents the results of the quantitative comparison.

As shown, removing either component leads to an increase in error, while removing both causes the CEP95 to rise significantly from 0.48 m/s to 2.54 m/s . These results demonstrate the effectiveness of the anomaly detection module in filtering out abnormal data.

H. Model Scale and Efficiency

To evaluate model complexity and inference efficiency, we compare MTIMNet with several baselines in terms of trainable parameters, inference time, and floating point operations (FLOPs) on a server device equipped with an NVIDIA GeForce RTX 3090, as shown in Table IX. The MTIMNet has 1.085 M parameters and 3.759 M FLOPs, lower than most baselines and close to the lightweight recent method AirIO. It also achieves the fastest CPU inference time (4.0 ms , tied with AirIO) and competitive GPU latency (4.0 ms), demonstrating a favorable trade-off between complexity, efficiency, and localization performance.

TABLE IX

COMPARISON OF MODEL COMPLEXITY AND INFERENCE TIME.

Model	Trainable Parameters ↓	Inference Time (CPU / GPU) ↓	FLOPs ↓
IONet	830.008 K	52.5 ms / 7.5 ms	33.830 M
RoNIN	4.438 M	9.0 ms / 5.5 ms	21.225 M
LLIO	7.158 M	8.5 ms / 6.5 ms	26.310 M
UniTS	2.451 M	27.5 ms / 13.0 ms	20.155 M
IMUNet	4.068 M	202.5 ms / 7.0 ms	97.733 M
EqNIO	4.361 M	43.0 ms / 12.5 ms	50.785 M
AirIO	897.186 K	4.0 ms / 2.5 ms	3.759 M
MTIMNet	1.085 M	4.0 ms / 4.0 ms	3.630 M

TABLE X

QUANTITATIVE COMPARISON OF MTIMNET WITH DIFFERENT PSEUDO WHEEL SPEED FUSION STRATEGIES ON FREE RIDING TRAJECTORIES.

	ATE	RTE	PDE	AYE
w/o pseudo wheel speed	13.5	13.83	0.06	1.86
w/ pseudo wheel speed (equal-weight fusion)	11.52	11.18	0.06	1.86
w/ pseudo wheel speed (inverse-variance weighted fusion)	10.81	10.35	0.06	1.86

I. Fusion Study

To validate the effectiveness of pseudo wheel speed (PWS) for drift calibration, we run MTIMNet on free riding trajectories and estimate PWS by continuously detecting valid pedalling periodicity. Once available, the PWS is converted into a displacement over the corresponding interval and fused with the MTIMNet displacement estimate using inverse-variance weighting. Table X compares three settings: without PWS, with equal-weight fusion, and with inverse-variance weighted fusion, where the MTIMNet variance is predicted by the model and the PWS variance is derived from the corresponding error standard deviation. The results show that PWS improves localization accuracy, and inverse-variance weighted fusion performs best, reducing the ATE from 13.50 m to 10.81 m . This demonstrates that PWS provides an effective auxiliary observation for reducing long-term drift.

VIII. CONCLUSION

This paper proposes an inertial-only bike tracking framework in environments where GNSS signals are blocked or unavailable. It employs an inertial motion estimation model based on the mixture-of-experts structure to infer the bike's trajectory, and estimates wheel speeds from the rider's periodic pedalling pattern to calibrate the estimates in real time. This enables large-scale GNSS-free device tracking and management for ride-hailing platforms. Future work will further investigate model distillation strategies to support deployment on embedded devices, integrate opportunistic signals such as Wi-Fi and 5G for additional calibration, and explore collaborative localization among multiple shared bikes to enhance localization performance in more complex urban environments.

REFERENCES

- [1] R. E. Kalman, "A new approach to linear filtering and prediction problems," *Journal of Fluids Engineering*, 1960.

- [2] J. Zhao, L. Zhang, K. Ye, J. Ye, J. Zhang, F. Zhang, and C. Xu, "Gltc: A metro passenger identification method across a/c data and sparse wifi data," *IEEE Transactions on Intelligent Transportation Systems*, vol. 23, no. 10, pp. 18337–18351, 2022.
- [3] Z. Luo, W. Li, Y. Wu, H. Dong, L. Bian, and W. Wang, "Accurate indoor localization for bluetooth low energy backscatter," *IEEE Internet of Things Journal*, vol. 12, no. 2, pp. 1805–1816, 2025.
- [4] T. Liu, B. Li, G. Chen, L. Yang, J. Qiao, and W. Chen, "Tightly coupled integration of gnss/uwb/vio for reliable and seamless positioning," *IEEE Transactions on Intelligent Transportation Systems*, vol. 25, no. 2, pp. 2116–2128, 2024.
- [5] C. Chen, X. Lu, A. Markham, and N. Trigoni, "Ionet: Learning to cure the curse of drift in inertial odometry," *Proceedings of the AAAI Conference on Artificial Intelligence*, vol. 32, no. 1, Apr. 2018. [Online]. Available: <https://ojs.aaai.org/index.php/AAAI/article/view/12102>
- [6] S. Herath, H. Yan, and Y. Furukawa, "Ronin: Robust neural inertial navigation in the wild: Benchmark, evaluations, & new methods," in *2020 IEEE International Conference on Robotics and Automation (ICRA)*, 2020, pp. 3146–3152.
- [7] Y. Wang, J. Kuang, X. Niu, and J. Liu, "Llio: Lightweight learned inertial odometry," *IEEE Internet of Things Journal*, vol. 10, no. 3, pp. 2508–2518, 2022.
- [8] P. Zhang, Z. Deng, Z. Meng, H. Li, J. Wang, and L. Wang, "Pedestrian inertial positioning method based on foot quasi-zero velocity observation under multiple motion modes," *IEEE Internet of Things Journal*, vol. 10, no. 20, pp. 18438–18447, 2023.
- [9] X. Xia, N. P. Bhatt, A. Khajepour, and E. Hashemi, "Integrated inertial-lidar-based map matching localization for varying environments," *IEEE Transactions on Intelligent Vehicles*, vol. 8, no. 10, pp. 4307–4318, 2023.
- [10] S. J. O'Bryan, N. A. Brown, F. Billaut, and D. M. Rouffet, "Changes in muscle coordination and power output during sprint cycling," *Neuroscience Letters*, vol. 576, pp. 11–16, 2014. [Online]. Available: <https://www.sciencedirect.com/science/article/pii/S0304394014003954>
- [11] C. Chen and X. Pan, "Deep learning for inertial positioning: A survey," *IEEE Transactions on Intelligent Transportation Systems*, 2024.
- [12] H. Chen, P. Aggarwal, T. M. Taha, and V. P. Chodavarapu, "Improving inertial sensor by reducing errors using deep learning methodology," in *NAECON 2018-IEEE National Aerospace and Electronics Conference*. IEEE, 2018, pp. 197–202.
- [13] R. Li, C. Fu, W. Yi, and X. Yi, "Calib-net: Calibrating the low-cost imu via deep convolutional neural network," *Frontiers in Robotics and AI*, vol. 8, p. 772583, 2022.
- [14] F. Nobre and C. Heckman, "Learning to calibrate: Reinforcement learning for guided calibration of visual-inertial rigs," *The International Journal of Robotics Research*, vol. 38, no. 12-13, pp. 1388–1402, 2019.
- [15] M. Brossard, S. Bonnabel, and A. Barrau, "Denoising imu gyroscopes with deep learning for open-loop attitude estimation," *IEEE Robotics and Automation Letters*, vol. 5, no. 3, pp. 4796–4803, 2020.
- [16] F. Huang, Z. Wang, L. Xing, and C. Gao, "A mems imu gyroscope calibration method based on deep learning," *IEEE Transactions on Instrumentation and Measurement*, vol. 71, pp. 1–9, 2022.
- [17] Y. Qiu, C. Wang, C. Xu, Y. Chen, X. Zhou, Y. Xia, and S. Scherer, "Airimu: Learning uncertainty propagation for inertial odometry," 2024. [Online]. Available: <https://arxiv.org/abs/2310.04874>
- [18] H. Yan, Q. Shan, and Y. Furukawa, "Ridi: Robust imu double integration," in *Proceedings of the European conference on computer vision (ECCV)*, 2018, pp. 621–636.
- [19] S. Cortés, A. Solin, and J. Kannala, "Deep learning based speed estimation for constraining strapdown inertial navigation on smartphones," in *2018 IEEE 28th International Workshop on Machine Learning for Signal Processing (MLSP)*. IEEE, 2018, pp. 1–6.
- [20] B. Zhou, Z. Gu, F. Gu, P. Wu, C. Yang, X. Liu, L. Li, Y. Li, and Q. Li, "Deepvip: Deep learning-based vehicle indoor positioning using smartphones," *IEEE Transactions on Vehicular Technology*, vol. 71, no. 12, pp. 13299–13309, 2022.
- [21] S. Herath, D. Caruso, C. Liu, Y. Chen, and Y. Furukawa, "Neural inertial localization," in *Proceedings of the IEEE/CVF Conference on Computer Vision and Pattern Recognition*, 2022, pp. 6604–6613.
- [22] S. Sun, D. Melamed, and K. Kitani, "Idol: Inertial deep orientation-estimation and localization," in *Proceedings of the AAAI Conference on Artificial Intelligence*, vol. 35, no. 7, 2021, pp. 6128–6137.
- [23] B. Rao, E. Kazemi, Y. Ding, D. M. Shila, F. M. Tucker, and L. Wang, "Ctin: Robust contextual transformer network for inertial navigation," in *Proceedings of the AAAI Conference on Artificial Intelligence*, vol. 36, no. 5, 2022, pp. 5413–5421.
- [24] R. K. Jayanth*, Y. Xu*, Z. Wang, E. Chatzipantazis, K. Daniilidis, and D. Gehrig, "EqNIO: Subequivariant neural inertial odometry," in *The Thirteenth International Conference on Learning Representations*, 2025. [Online]. Available: <https://openreview.net/forum?id=C8jXEugWkq>
- [25] S. Zhao, S. Zhou, R. Blanchard, Y. Qiu, W. Wang, and S. Scherer, "Tartan imu: A light foundation model for inertial positioning in robotics," in *2025 IEEE/CVF Conference on Computer Vision and Pattern Recognition (CVPR)*, 2025, pp. 22520–22529.
- [26] W. Liu, D. Caruso, E. Ilg, J. Dong, A. I. Mourikis, K. Daniilidis, V. Kumar, and J. Engel, "Tlio: Tight learned inertial odometry," *IEEE Robotics and Automation Letters*, vol. 5, no. 4, pp. 5653–5660, 2020.
- [27] B. Zeinali, H. Zanddzari, and M. J. Chang, "Imunet: Efficient regression architecture for inertial imu navigation and positioning," *IEEE Transactions on Instrumentation and Measurement*, vol. 73, pp. 1–13, 2024.
- [28] Y. Qiu, C. Xu, Y. Chen, S. Zhao, J. Geng, and S. Scherer, "Airio: Learning inertial odometry with enhanced imu feature observability," *IEEE Robotics and Automation Letters*, vol. 10, no. 9, pp. 9368–9375, 2025.
- [29] G. Cioffi, L. Bauersfeld, E. Kaufmann, and D. Scaramuzza, "Learned inertial odometry for autonomous drone racing," *IEEE Robotics and Automation Letters*, vol. 8, no. 5, pp. 2684–2691, 2023.
- [30] Y. Sun, W. Wang, L. Mottola, J. Zhang, R. Wang, and Y. He, "Indoor drone localization and tracking based on acoustic inertial measurement," *IEEE Transactions on Mobile Computing*, vol. 23, no. 6, pp. 7537–7551, 2024.
- [31] S. Lu, Y. Gong, H. Luo, F. Zhao, Z. Li, and J. Jiang, "Heterogeneous multi-task learning for multiple pseudo-measurement estimation to bridge gps outages," *IEEE Transactions on Instrumentation and Measurement*, vol. 70, pp. 1–16, 2020.
- [32] Y. Wang, W. Song, Y. Wang, X. Dai, and Y. Lou, "Metroloc: Metro vehicle mapping and localization with lidar-camera-inertial integration," *IEEE Transactions on Intelligent Transportation Systems*, vol. 26, no. 2, pp. 1441–1453, 2025.
- [33] J. Wang, P. Gu, L. Wang, and Z. Meng, "Rvio: An effective localization algorithm for range-aided visual-inertial odometry system," *IEEE Transactions on Intelligent Transportation Systems*, vol. 25, no. 2, pp. 1476–1490, 2024.
- [34] Y. Huang, P. Li, S. Ma, S. Yan, M. Tan, J. Yu, and Z. Wu, "Visual-inertial-acoustic sensor fusion for accurate autonomous localization of underwater vehicles," *IEEE Transactions on Cybernetics*, 2024.
- [35] S. Bai, W. Wen, Y. Li, C. Shi, and L.-T. Hsu, "Toward persistent spatial awareness: A review of pedestrian dead reckoning-centric indoor positioning with smartphones," *IEEE Transactions on Instrumentation and Measurement*, vol. 73, pp. 1–28, 2024.
- [36] F. Elyasi and R. Manduchi, "Step length is a more reliable measurement than walking speed for pedestrian dead-reckoning*," in *2023 13th International Conference on Indoor Positioning and Indoor Navigation (IPIN)*, 2023, pp. 1–6.
- [37] X. Shi, Z. Wang, H. Zhao, S. Qiu, R. Liu, F. Lin, and K. Tang, "Threshold-free phase segmentation and zero velocity detection for gait analysis using foot-mounted inertial sensors," *IEEE Transactions on Human-Machine Systems*, vol. 53, no. 1, pp. 176–186, 2023.
- [38] X. Zhang and J. Yang, "An adaptive robust ekf based on mahalanobis distance and non-holonomic constraints for enhancing vehicle positioning accuracy," *IEEE Sensors Journal*, 2024.
- [39] C. Chen, C. X. Lu, J. Wahlström, A. Markham, and N. Trigoni, "Deep neural network based inertial odometry using low-cost inertial measurement units," *IEEE Transactions on Mobile Computing*, vol. 20, no. 4, pp. 1351–1364, 2019.
- [40] J. Ma, Z. Zhao, X. Yi, J. Chen, L. Hong, and E. H. Chi, "Modeling task relationships in multi-task learning with multi-gate mixture-of-experts," in *Proceedings of the 24th ACM SIGKDD International Conference on Knowledge Discovery & Data Mining*, ser. KDD '18. New York, NY, USA: Association for Computing Machinery, 2018, p. 1930–1939. [Online]. Available: <https://doi.org/10.1145/3219819.3220007>
- [41] A. Kendall and Y. Gal, "What uncertainties do we need in bayesian deep learning for computer vision?" in *Proceedings of the 31st International Conference on Neural Information Processing Systems*, ser. NIPS'17. Red Hook, NY, USA: Curran Associates Inc., 2017, p. 5580–5590.
- [42] S. Butterworth *et al.*, "On the theory of filter amplifiers," *Wireless Engineer*, vol. 7, no. 6, pp. 536–541, 1930.
- [43] H. Ying, C. Silex, A. Schnitzer, S. Leonhardt, and M. Schiek, "Automatic step detection in the accelerometer signal," in *4th International Workshop on Wearable and Implantable Body Sensor Networks (BSN 2007) March 26–28, 2007 RWTH Aachen University, Germany*. Springer, 2007, pp. 80–85.
- [44] G. E. Box, G. M. Jenkins, G. C. Reinsel, and G. M. Ljung, *Time series analysis: forecasting and control*. John Wiley & Sons, 2015.

- [45] S. Li, R. R. Chowdhury, J. Shang, R. K. Gupta, and D. Hong, "Units: Short-time fourier inspired neural networks for sensory time series classification," in *Proceedings of the 19th ACM Conference on Embedded Networked Sensor Systems*, ser. SenSys '21. New York, NY, USA: Association for Computing Machinery, 2021, p. 234–247. [Online]. Available: <https://doi.org/10.1145/3485730.3485942>
- [46] F. Liu, H. Ge, D. Tao, R. Gao, and Z. Zhang, "Smartphone-based pedestrian inertial tracking: Dataset, model, and deployment," *IEEE Transactions on Instrumentation and Measurement*, vol. 73, pp. 1–13, 2024.
- [47] J. Sturm, N. Engelhard, F. Endres, W. Burgard, and D. Cremers, "A benchmark for the evaluation of rgb-d slam systems," in *2012 IEEE/RSJ International Conference on Intelligent Robots and Systems*, 2012, pp. 573–580.



Qun Li is the Head of DiDi Research Outreach, is leading DiDi's efforts to work together with academic institutions worldwide, including research collaboration, talent cultivation and academic exchange. She was in the organizing committee of several workshops and tutorials. Her research interests lie in the intersection of artificial intelligence, autonomous driving and computer vision.



Feng Liu received the B.S. degree from the Inner Mongolia University of Technology, Inner Mongolia, China, in 2022. He is currently working towards the Ph.D. degree in software engineering at Beijing Jiaotong University, China. His research interests include multi-target positioning and mobile computing.



Guobin Wu is the Director of Technology Ecology and Development Department at DiDi. His research interests include artificial intelligence and computer vision.



Kejia Li received the B.S. degree in software engineering from Beijing Jiaotong University, Beijing, China, in 2024. He is currently pursuing the integrated M.S. and Ph.D. degree in the School of Cyberspace Security at Beijing Jiaotong University, Beijing, China. His research interests include filtering algorithms, inertial navigation, and mobile computing.



Qiang Ni is currently a Professor and the Head of the Communication Systems Group, School of Computing and Communications, Lancaster University, Lancaster, U.K. His research interests include the area of future generation communications, computing and networking, including green communications and mobile networking, 5G and 6G, SDN, cloud networks, mobile computing, IoTs, cyber physical systems, AI, machine learning, big data analytics, and vehicular networks.



Zhiwei Yang received his Bachelor of Science degree in computer science from Liaoning Petrochemical University, China, in 2005. He currently serves as an Embedded Systems Expert in the Two-Wheeler Sharing Department at DiDi. His research interests focus on positioning and sensor technologies, particularly their application to low-cost devices.



Chunwei Yang received the MS degree from Zhejiang University, China, in 2016. He is currently the embedded software expert with the Hardware R&D Department, DiDi Company. His research interests include positioning, machine learning, and deep learning.



Ruipeng Gao received the B.S. degree from the Beijing University of Posts and Telecommunications, China, in 2010, and the Ph.D. degree from Peking University, China, in 2016. He was a Visiting Scholar with Purdue University, USA, in 2019. He is currently a Professor with the School of Cyberspace Science and Technology, Beijing Jiaotong University, China. His research interests include mobile computing and applications.